

Sources and Pathways of Intraseasonal Meridional Kinetic Energy in the Equatorial Atlantic Ocean

MAREIKE KÖRNER,^a MARTIN CLAUS,^{a,b} PETER BRANDT,^{a,b} AND FRANZ PHILIP TUCHEN^a

^a *GEOMAR Helmholtz Centre for Ocean Research Kiel, Kiel, Germany*

^b *Faculty of Mathematics and Natural Science, Kiel University, Kiel, Germany*

(Manuscript received 22 December 2021, in final form 8 July 2022)

ABSTRACT: In the equatorial Atlantic Ocean, meridional velocity variability exhibits a pronounced peak on intraseasonal time scales whereas zonal velocity dominantly varies on seasonal to interannual time scales. We focus on the intraseasonal meridional velocity variability away from the near-surface layer, its source regions, and its pathways into the deep ocean. This deep intraseasonal velocity variability plays a key role in equatorial dynamics as it is an important energy source for the deep equatorial circulation. The results are based on the output of a high-resolution ocean model revealing intraseasonal energy levels along the equator at all depths that are in good agreement with shipboard and moored velocity data. Spectral analyses reveal a pronounced signal of intraseasonal Yanai waves with westward phase velocities and zonal wavelengths longer than 450 km. Different sources and characteristics of these Yanai waves are identified: near the surface between 40° and 10°W, low-baroclinic-mode Yanai waves with periods of around 30 days are excited. These waves have a strong seasonal cycle with a maximum in August. High-frequency Yanai waves (10–20-day period) are excited at the surface east of 10°W. In the region between the North Brazil Current and the Equatorial Undercurrent, high-baroclinic-mode Yanai waves with periods between 30 and 40 days are generated. Yanai waves with longer periods (40–80 days) are shed from the deep western boundary current. The Yanai wave energy is carried along beams eastward and downward, thus explaining differences in strength, structure, and periodicity of the meridional intraseasonal variability in the equatorial Atlantic Ocean.

SIGNIFICANCE STATEMENT: Past studies show that intraseasonal meridional kinetic energy is important for the deep equatorial circulation (DEC). However, numerical studies use intraseasonal variability with varying characteristics to investigate the formation and maintenance of the DEC. This is partly because of sparse observations at depth that are limited to single locations. This study investigates intraseasonal meridional kinetic energy in the equatorial Atlantic in a high-resolution ocean model that is tested against available shipboard and moored observations. We analyze the spatial and temporal distribution and the baroclinic structure of intraseasonal variability. Using the model, we identify different sources and pathways of intraseasonal energy in the deep equatorial Atlantic. We offer groundwork for further studies on the formation and maintenance of the DEC.

KEYWORDS: Atlantic Ocean; Tropics; Ocean dynamics; Intraseasonal variability; Oceanic waves; Internal waves

1. Introduction

The equatorial circulation of the Atlantic Ocean is characterized by a complex set of energetic zonal currents that vary on seasonal to interannual time scales (Brandt et al. 2016). However, meridional velocity variability exceeds zonal velocity variability at intraseasonal time scales with enhanced variability in the period range from 10 to 50 days (Athie and Marin 2008; Bunge et al. 2008; Tuchen et al. 2018).

In the upper ocean, tropical instability waves (TIWs) are the prevalent source of intraseasonal variability (Weisberg and Weingartner 1988; Jochum et al. 2004; Athie and Marin 2008; von Schuckmann et al. 2008; Perez et al. 2012; Tuchen

et al. 2018). TIWs can be detected from satellite due to their signature in sea surface temperature (SST), sea surface salinity, and sea level anomaly (e.g., Olivier et al. 2020). In the Atlantic, TIWs typically have periods between 20 and 60 days, their zonal wavelengths range from 600 to 1200 km, and they propagate westward with a phase speed of 20–60 cm s⁻¹ (Weisberg and Weingartner 1988; Athie and Marin 2008; von Schuckmann et al. 2008). In addition to the TIWs at the surface, sea surface height variability exists in the equatorial Pacific on intraseasonal time scales that can be explained by low-baroclinic-mode/barotropic Rossby waves (Farrar and Weller 2006; Farrar 2011). These waves propagate away from the equator and can be traced to at least 30°N (Farrar et al. 2021).

Baroclinic and barotropic instability is responsible for the formation of TIWs (Grodsky et al. 2005; von Schuckmann et al. 2008). North of the equator, it is the barotropic instability due to horizontal shear between the Equatorial Undercurrent (EUC) and the northern branch of the South Equatorial Current (nSEC), as well as between the nSEC and the North Equatorial Countercurrent. Additionally, baroclinic instability due to vertical shear within the nSEC contributes. South of the equator, baroclinic instability originating from the vertical shear

Denotes content that is immediately available upon publication as open access.

Tuchen's current affiliation: NOAA/Atlantic Oceanographic and Meteorological Laboratory, Miami, Florida.

Corresponding author: Mareike Körner, mkoerner@geomar.de

DOI: 10.1175/JPO-D-21-0315.1

© 2022 American Meteorological Society. For information regarding reuse of this content and general copyright information, consult the AMS Copyright Policy (www.ametsoc.org/PUBSReuseLicenses).

of the central branch of the South Equatorial Current generates TIWs as well (von Schuckmann et al. 2008).

TIWs undergo a strong seasonal modulation that originates from the seasonal cycle of equatorial winds. In June/July the southeasterly trade winds intensify at the equator. With it, the near-surface circulation, as well as the instability of the zonal currents, intensifies accordingly, resulting in a peak of TIW energy in boreal summer (Weisberg and Weingartner 1988; Athie and Marin 2008; von Schuckmann et al. 2008; Tuchen et al. 2018).

On shorter time scales than those of TIWs, another source of intraseasonal variability is biweekly wind fluctuations that directly excite biweekly Yanai waves with long zonal wavelengths (Athie and Marin 2008). The signal of the meridional wind fluctuations is present all year long. However, during boreal spring and summer, when a strong SST front develops in the eastern equatorial Atlantic, the air–sea interactions between atmospheric wind forcing and the feedback due to advection of warm and cold SST anomalies support a substantial part of the biweekly variability (de Coëtlogon et al. 2010).

Enhanced intraseasonal variability is also observed at greater depths (Bunge et al. 2008; Tuchen et al. 2018; Zhang et al. 2020). Tuchen et al. (2018) analyzed meridional velocity data from a mooring site at the equator at 23°W. Their results suggest that TIWs excite Yanai waves of modes 2–5 with 30–40-day period, which propagate their energy downward and eastward. This intraseasonal energy can be traced from the surface down to about 2000 m. Nevertheless, the study also found signals of intraseasonal Yanai waves that cannot be explained by sources of wave energy at the surface. Instead, the deep western boundary current (DWBC) was suggested as another source region for the generation of intraseasonal Yanai waves. From moored observations in the equatorial Pacific Ocean, Zhang et al. (2020) found intraseasonal variability that can be associated with short Rossby waves with westward phase speed that propagate their energy southeastward and downward.

The energy of intraseasonal variability is thought to play an important role in equatorial dynamics. At depth, the so-called deep equatorial circulation (DEC) exists. The DEC consists of high-baroclinic-mode equatorial deep jets (EDJs) and low-baroclinic-mode or barotropic equatorial intermediate current system (EICS) also called extra-equatorial jets (EEJs) (Ascani et al. 2010, 2015; Cravatte et al. 2012, 2017; Ménesguen et al. 2019; Delpech et al. 2020, 2021). EDJs are vertically stacked jets with a periodicity of about 4.5 years (Johnson and Zhang 2003; Youngs and Johnson 2015; Claus et al. 2016). EDJs are the dominant source of interannual variability at intermediate depths in the equatorial Atlantic and they are suggested to affect climate variability (Brandt et al. 2011). Model studies suggest that the deep equatorial intraseasonal variability (DEIV) plays an important role in the formation of the DEC (d’Orgeville et al. 2007; Hua et al. 2008; Ascani et al. 2010, 2015).

From the results of numerical simulations, Ascani et al. (2010) found that the EICS can be generated by strong intraseasonal Yanai waves through self-advection and dissipation west of the Yanai beam that carries energy from the surface eastward and downward. The shear instability of short, low-baroclinic-mode Yanai waves generated near the western boundary of the equatorial ocean was found to be responsible

for the formation of EDJs (d’Orgeville et al. 2007; Hua et al. 2008). In contrast, in the simulations of Ascani et al. (2015), DEIV is generated in the upper ocean, propagates downward and rectifies into the low-frequency EDJs. Their solution largely depends on the structure and amplitude of the DEIV. Greatbatch et al. (2018) showed how intraseasonal waves can maintain EDJs against dissipation: a zonal jet of smaller meridional scale distorts an intraseasonal wave of larger meridional scale such that it leads to a convergence of the meridional flux of zonal momentum. Recently, Bastin et al. (2020) showed in an idealized model setup that EDJs are generated when the model is driven only by the convergence of the meridional flux of intraseasonal zonal momentum. This underlines the importance of understanding the DEIV in order to realistically model the EDJs. Furthermore, Delpech et al. (2021) proposed that intraseasonal barotropic Rossby waves are important for the generation of the EEJs.

Intraseasonal variability in the deep equatorial Atlantic Ocean has been analyzed from moored velocity observations that are limited to single locations along the equator (Bunge et al. 2008; Tuchen et al. 2018). We want to extend these analyses by making use of a high-resolution ocean model that is tested against an extended dataset of shipboard and moored observations. The goal of this study is to characterize the deep intraseasonal variability along the equator in the Atlantic Ocean.

This study is structured as follows: section 2 introduces the model as well as the observational data used to validate the model. Section 3 presents the methods. Similarities and differences between observations and model results are described in section 4. In section 5 we describe the characteristics of intraseasonal variability. We then discuss energy sources and pathways of intraseasonal variability in section 6. Section 7 provides a summary and a discussion.

2. Data

a. Model

To analyze intraseasonal variability in the equatorial Atlantic Ocean we use the output of a numerical ocean model. We utilize the VIKING20X model, which consists of a global host model with a high-resolution nest of the Atlantic Ocean. For a detailed description of the model, the reader is referred to Biastoch et al. (2021), where the configuration we use is called VIKING20X-JRA-short.

The simulation is based on the Nucleus for European Modelling of the Ocean (NEMO: Madec and NEMO Team 2016) code, version 3.6. The global host model ORCA025 has a horizontal resolution of 0.25°. It has 46 depth layers whose vertical extents range from 6 m at the surface to ~250 m at depth. The high-resolution nest covers the Atlantic Ocean from 33.5°S to ~65°N. Its horizontal resolution is 1/20°, whereas the vertical resolution is the same as the global ORCA025 configuration.

The atmospheric forcing for the ocean-only model is provided by the JRA-55-do dataset, version 1.4 (Tsujino et al. 2018). The atmospheric forcing field is available on a 0.5° horizontal grid at 3-hourly temporal resolution. It is interpolated to the horizontal resolution of the host and the nest grid. The model configuration

we use is integrated between the years 1980 and 2018 (38 years). The output is saved at a daily resolution.

b. Observation

The model output is compared with observations to validate the representation of intraseasonal variability. To do so we use the moored velocity observations at seven different locations along the equator. An overview of the data availability as a function of time and depth at each mooring location can be found in [appendix A \(Fig. A1\)](#). Note that except for the mooring at 0°, 23°W the measurements at depth are relatively sparse.

Single-point current meters installed in two moorings located at the continental slope of the western boundary at 0.4°N, 44.25°W and 0.2°N, 44.3°W collected data from October 1990 to September 1991 and from October 1992 to March 1994, respectively. In [Fischer and Schott \(1997\)](#), a detailed description of the dataset can be found. Note that additionally an acoustic Doppler current profiler (ADCP) was installed at the mooring at 0.2°N, 44.3°W. However, as it only recorded data for 110 days, we did not use these data for this study.

Four moored single-point current meters collected data at 0°, 36°W between October 1992 and May 1994 ([Send et al. 2002](#)). At 0°, 35°W velocity data were recorded from August 2004 to June 2006 using an ADCP and single-point current meters ([Hormann and Brandt 2009](#)).

The mooring dataset at 0°, 23°W we use is an update of [Tuchen et al. \(2018\)](#) extended by three mooring periods. The updated moored velocity dataset additionally includes near-surface velocity observations from a single-point current meter installed at 10–12 m as part of the PIRATA buoy at 0°, 23°W ([Tuchen et al. 2022](#)). The mooring provides velocity measurements from December 2001 to June 2021 (apart from a period from December 2002 to February 2004 when no mooring was in place).

From May 2003 to March 2019 velocity was measured at 0°, 10°W using ADCPs and single-point current meter. However, the mooring was not consecutively installed, leading to data gaps of up to 2 years. For the data measured prior to June 2005, the reader is referred to [Bunge et al. \(2008\)](#). The data afterward are described in [Brandt et al. \(2021\)](#). At 0°, 0° velocity data were recorded by ADCPs between October 2007 and May 2011 ([Johns et al. 2014](#)).

We also compare snapshots of meridional velocity from the model with an observed equatorial section of meridional velocity. This section was measured along the equator between 29 September 2019 and 22 October 2019 from east to west in the course of the research cruise M158 conducted by the research vessel (R/V) *Meteor* ([Brandt et al. 2019](#)). The velocity profiles were obtained from ADCP measurements with two instruments attached to the CTD rosette and lowered from the surface to 6000 m or close to the bottom. The horizontal resolution of the velocity profiles is 1° from 5°E to 35°W. West of 35°W the resolution increases toward the western boundary.

3. Methods

a. Lanczos filter

In the course of this study time series of velocity are filtered for variability on intraseasonal time scales, which we define as

variability with periods shorter than 80 days. For that purpose, a cosine-Lanczos filter as formulated by [Thomson and Emery \(2014\)](#) with a cutoff frequency of 1/80 cycles per day and a window length of 185 days is used.

b. Modal decomposition

The concept of standing vertical normal modes is an appealing way to describe the vertical structure of the ocean ([Gill 1982](#)). It is especially useful when describing linear wave dynamics. Wave characteristics derived for the homogeneous ocean can be transferred to the stratified ocean using normal modes. For that, we fit vertical profiles of horizontal velocity to a set of vertical normal modes. Note that for a wave to consist of one baroclinic mode alone, the wave has to reflect from the bottom and return to the surface within the forcing region, thus creating a vertically standing wave. The waves discussed in this study mostly do not fulfill this requirement. However, the velocity field can still be decomposed into vertical normal modes. To fully describe the waves, a spectrum of vertical normal modes is needed. The modal decomposition then helps in characterizing these waves as it reveals what part of the vertical mode spectrum is elevated for the respective waves ([Philander 1978](#)).

The normal modes are based on a mean buoyancy frequency profile N^2 acquired by averaging N^2 between 5°N and 5°S. The eigenvalue problem

$$\frac{d}{dz} \left(\frac{1}{N^2} \frac{d\hat{p}}{dz} \right) + \frac{1}{c_n^2} = 0 \quad (1)$$

can be derived from the governing equations for an incompressible, inviscid fluid in a nonrotating system linearized about a state of rest. Solving the eigenvalue problem for a vertical mode n gives the structure function \hat{p} ([Gill 1982](#)), where c_n is the gravity wave speed for the vertical mode n . The eigenvalue problem has two boundary conditions:

$$\hat{p} + \frac{g}{N^2} \frac{d\hat{p}}{dz} = 0 \quad \text{at } z = 0 \quad \text{and} \quad \frac{1}{N^2} \frac{d\hat{p}}{dz} = 0 \quad \text{at } z = -H,$$

where H is the full water depth of the buoyancy frequency profile (here we use $H = 5875$ m). We normalize the amplitude of each vertical structure function such that

$$\int_{-H}^0 \hat{p}_n \hat{p}_m dz = \delta_{nm} H, \quad (2)$$

where δ_{nm} is the Kronecker delta.

In a next step, the horizontal velocities are fit to the structure functions. The horizontal velocities at one location can be expressed as $u(z, t) = \mathbf{A} \tilde{u}(n, t)$, where $A_{ij} = \hat{p}_j(z_i)/(g\rho_0) \in \mathbb{R}^{Z \times N}$ with Z being the number of vertical levels and N being the number of normal modes. In our case N is 16 as we consider the first 16 vertical normal modes (including the barotropic mode). The modal velocities are then $\tilde{u}(n, t) = \mathbf{A}^{-1} u(z, t)$ with \mathbf{A}^{-1} being the inverse of \mathbf{A} . One issue of this fitting is the topography. The modal structures are calculated using a full depth N^2 profile. However, the velocity profiles reach

different depths depending on their location. Thus, we have to perform the fitting in presence of topography. To resolve this issue, we cut the structure function to the depth of the respective locations. Consequently, the matrix \mathbf{A} is not invertible as there is no unique solution to the linear system. To find the best solution for our application we calculate the solution using a ridge regression. The ridge regression works by minimizing a penalized residual sum of squares:

$$\min_{\tilde{u}} \|\mathbf{A}\tilde{u} - u\|_2^2 + \alpha \|\tilde{u}\|_2^2, \quad (3)$$

where $\alpha > 0$ is a hyperparameter for tuning the solution. Note that this system can also be solved using an ordinary least squares method. However, as the system is highly under-constrained in shallow locations, compensating effects lead to unrealistic high modal amplitudes. By using the ridge regression, we can prohibit this behavior by choosing α accordingly. Choosing α is an optimization problem: for $\alpha \rightarrow 0$, we have little energy loss when transforming the modal velocities back to physical space, but at the same time we have unrealistic high modal velocities. For $\alpha \rightarrow \infty$, the ridge regression dampens the system, and we have high energy loss when transforming the modal velocities back to space. To find the optimal α , we use leave-one-out cross validation, that is, we separate the data into training and test data by marking a single sample as test data, leading to as many test sets as samples. The ridge regression is performed on all of these training sets and the α with the highest average score $R^2 = 1 - x/y$, computed on the corresponding test set, is chosen where x is the residual sum of squares and y is the total sum of squares. We find the optimal α for three locations with different depths: 29 (shallowest location away from the boundaries), 36, and 46 depth levels. The optimal α are 24.6, 23.1, and 21.5 with a score of 0.79, 0.8, and 0.81, respectively. As α does not vary much between the different depths and as the compensation effects are largest for shallow profiles, we choose α to be 24.6 for the fitting at all locations. Note that the fitting procedure using the ridge regression still leads to an energy loss of $\sim 10\%$ when transforming the velocities back to physical space.

c. Spectral analysis

To calculate spectral estimate of velocity time series, we use the method of Welch (1967). This method improves the spectral estimator by sectioning the time series using a Hanning window. The spectrum is then calculated for each section before averaging them. For the spectra of modeled meridional velocity at each grid point along the equator we use a window length of 5 years with a window overlap of 50%.

To calculate the spectrum of gappy moored velocity data at 0° , 23°W we apply the method of Lomb–Scargle. For details about this method see Tuchen et al. (2018).

To analyze the dominant periodicity of intraseasonal meridional velocity variability of observed moored velocity data we calculate spectral estimates and determine the period with maximum energy in the spectra. To calculate the spectra of meridional velocity at all mooring sites introduced in section 2b except at 0° , 23°W , we use the Welch method with a window

length of 1 year and an overlap of 50%. Note that the moored ADCP data at 0° , 10°W have gaps. Here we calculated the spectra for each mooring period individually. Afterward, we determine the period with maximum energy in the spectra on intraseasonal time scales. We average the periods over all mooring periods with a weighted mean based on the length of the mooring periods.

1) FREQUENCY–WAVENUMBER ANALYSIS

We analyze the equatorial wave field by calculating frequency–wavenumber spectra of modal velocity. To do so, we calculate spectra as a function of zonal wavenumber and frequency using a two-dimensional Fourier transform. We compare the spectra with theoretical dispersion relations of free equatorial waves. The wave *ansatz* of the theoretical dispersion relations has an opposing sign $[e^{i(kx - \omega t)}]$. Thus, the two-dimensional Fourier transform is defined accordingly:

$$X_{kj} = \sum_{m=0}^{M-1} \sum_{n=0}^{N-1} x_{mn} \exp \left[-2\pi i \left(\frac{mj}{M} - \frac{nk}{N} \right) \right] \quad \text{for } k = 0, \dots, N-1, \\ j = 0, \dots, M-1, \quad (4)$$

where m is the spatial dimension and n the temporal dimension.

Considering the conservation of energy while transforming the signal and the symmetry of real-valued Fourier transforms, we derive

$$\hat{S} = \frac{2}{NM} |X_{kj}|^2 \quad (5)$$

for the frequency–wavenumber spectral estimate.

Frequency–wavenumber spectra are calculated for modal velocities at the equator (longitude–time sections). To reduce the variance of the spectral estimator, the spectra are calculated on the $1/20^\circ$ grid between 0.25°S and 0.25°N individually and averaged afterward.

2) YANAI WAVE FILTER

The frequency–wavenumber spectra of the meridional modal velocity of all modes show a dominant signal of Yanai waves with westward phase velocity (see section 5a). To analyze the Yanai waves in greater detail, we filter the modal velocities for their signal. This filtering strategy follows the method of Farrar (2011). The basic idea of the filter is to isolate frequencies and wavenumbers of interest and transform them back into the longitude–time domain. Thus, frequency–wavenumber spectra pose as a basis for the Yanai-wave filter. For our case, we define a box around the theoretical dispersion relation of Yanai waves of the respective mode. All frequencies in a distance of 2.5 cycles per year of the theoretical dispersion relation are selected. Additionally, only wavenumbers between -0.25 and -0.01 cycles per degree are chosen. After defining the box, the spectra outside of it are set to zero. Subsequently, the inverse discrete Fourier transform is calculated to transform the spectra back to physical space. In analogy to calculating the frequency–wavenumber spectra, the Yanai-wave filtered modal velocities are calculated from

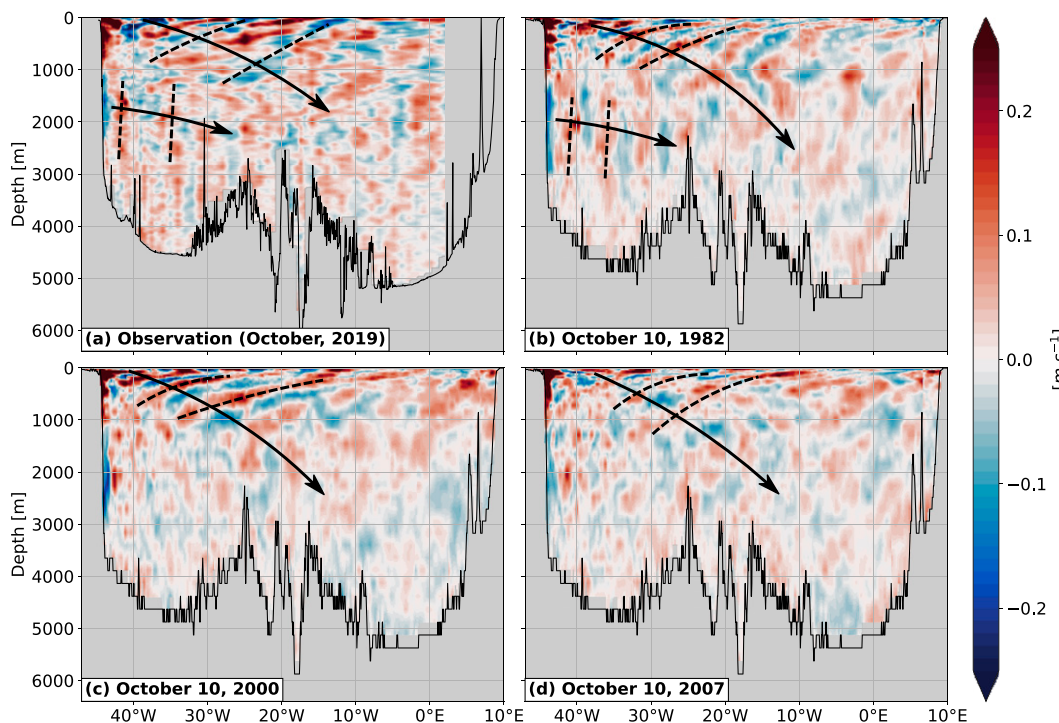


FIG. 1. (a) Meridional velocity (m s^{-1}) along the equator, measured during research cruise M158 of R/V *Meteor* between 29 Sep and 22 Oct 2019 from east to west. Also shown are snapshots of modeled meridional velocity from 10 Oct of the years (b) 1982, (c) 2000, and (d) 2007. Dashed black lines mark wave fronts. Solid black arrows show the proposed energy propagation path.

spectra between 0.25°S and 0.25°N separately and averaged afterward to increase statistical robustness. Farrar (2011) applies a two-dimensional Tukey window to the spectrum inside the box to reduce filter sidelobes. For our results the usage of the window function did not alter the results. We therefore abstain from using the Tukey window.

d. Ray tracing

The moored observations at 0° , 23°W show meridional velocity signals with upward phase propagation (Tuchen et al. 2018), which imply, following linear wave theory, a downward energy propagation (Gill 1982). These signals have been associated with intraseasonal Yanai waves (Ascani et al. 2010; Tuchen et al. 2018). The theoretical work of McCreary (1984) derived the slope of vertically propagating equatorial waves. The angle of propagation $\gamma(z)$ depends on only the angular wave frequency $\omega = 2\pi f$, the buoyancy frequency profile $N(z)$, and the meridional mode l :

$$\tan(\gamma) = \frac{c_{gz}}{c_{gx}} = \pm \frac{(2l+1)\omega}{N}, \quad (6)$$

where c_{gx} and c_{gz} are the zonal and vertical group velocities, $l = -1$ represents Kelvin waves, $l = 0$ represents Yanai waves, and $l = 1, 2, 3, \dots$ represent Rossby and gravity waves. Note that within the framework of vertical normal mode decomposition, vertical wave propagation can only exist by a superposition

of multiple vertical modes. The group velocity of such waves depends on the dominant mode contributing to its formation (Tuchen et al. 2018).

4. Model validation

We evaluate how well intraseasonal variability is simulated by comparing the model output with observations. Previous studies have shown that, at the equator, the kinetic energy in the intraseasonal frequency band is predominantly due to the meridional velocity variability whereas zonal velocity variability is found mostly on longer, seasonal to interannual time scales (Athie and Marin 2008; Bunge et al. 2008; Ascani et al. 2015; Tuchen et al. 2018). We therefore focus on the meridional velocity component to validate the modeled intraseasonal variability.

In a first step, we qualitatively compare an observed equatorial section of meridional velocity with snapshots of meridional velocity from the model output (Fig. 1). Note that the shipboard velocity section was measured in the course of 23 days. Measured velocity structures can thus appear distorted. In the observed velocity field, waves are identifiable that propagate their energy from the upper ocean at the western boundary eastward and downward (indicated by black arrows). Below 1000 m depth, the signals lose coherence and become weaker. The three snapshots of meridional velocity from the model output taken in the same season as the observed section exhibit similar structures in the upper ocean (Figs. 1b–d). In 2000 and 1982 the amplitude of the wave

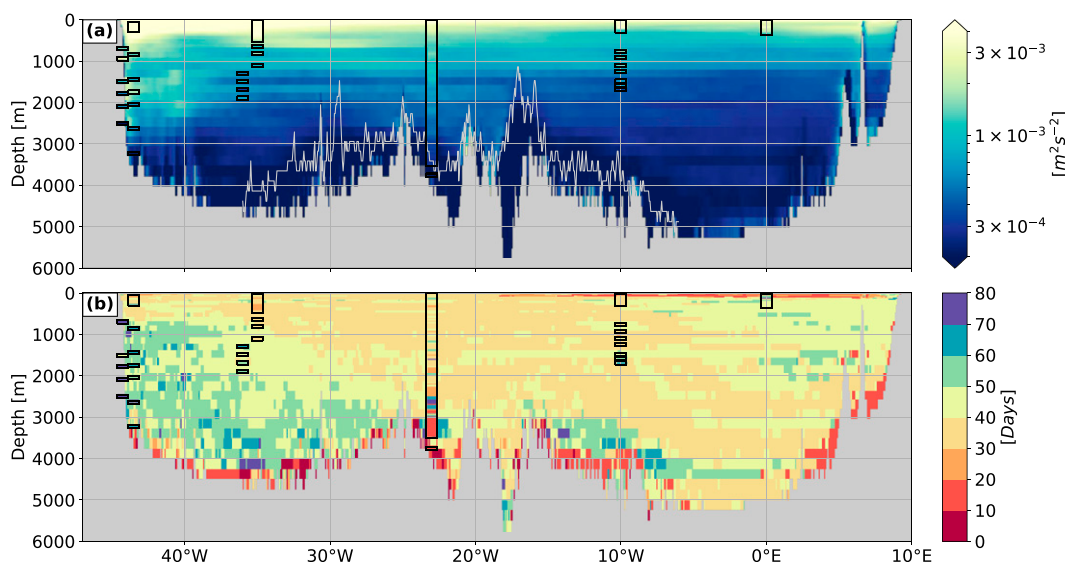


FIG. 2. (a) Equatorial section of mean intraseasonal kinetic energy of meridional velocity ($\text{m}^2 \text{s}^{-2}$). Intraseasonal is defined as variability with periods shorter than 80 days. Meridional kinetic energy is averaged over the whole model run. The gray line shows the minimum water depth between 1°S and 1°N in the longitude range of the Mid-Atlantic Ridge. (b) Period of the maximum energy of meridional velocity spectra in the intraseasonal frequency band. In (a) and (b) colored areas within black boxes show results of observed moored velocity data.

structure is strong and compares well to the amplitude in the observations. In 2007, the meridional velocity field in the upper ocean is, instead, much weaker and noisier. In the western part of the basin, observed velocity structures of large vertical extent are recognizable below 1000 m. Such structures are also visible in the snapshot of modeled meridional velocity in 1982. In 2000 and 2007 the amplitude of meridional velocity is weaker and no clear structures are recognizable. Overall, the observed meridional velocity section and three snapshots of the modeled meridional velocity compare well in structure and amplitude. The three snapshots furthermore suggest a strong year-to-year variability of meridional velocity fluctuations.

In a next step, we use moored velocity data at seven different locations to further validate the model's representation of intraseasonal meridional velocity variability. Note that the data coverage is mostly sparse and that the amount of data varies strongly between the different mooring locations (see Fig. A1 in appendix A). Figure 2a shows the modeled equatorial section of mean intraseasonal meridional kinetic energy averaged over the whole model run. The observed mean intraseasonal meridional kinetic energy at the individual mooring locations is superimposed. Overall, the modeled amplitudes fit well to the observed amplitudes. The upper ocean exhibits high intraseasonal energy levels declining with depth. Elevated intraseasonal energy levels are also found in both model and observations around the DWBC. Comparing the profiles of modeled and observed mean intraseasonal meridional kinetic energy at the mooring location individually allows for a closer inspection of the amplitude (Fig. B1 in appendix B). These reveal shortcomings of the model that include missing subsurface energy maxima at 0°, 35°W; 0°, 10°W; and 0°, 0°. Additionally, the intraseasonal energy levels tend to be stronger in the observation.

The periods with maximum energy in the meridional velocity spectra on intraseasonal time scales both in the model and in moored velocity data are presented in Fig. 2b. In general, the periodicity of modeled and observed meridional velocity variability agree well. The model shows that periods above 50 days dominate the variability in the western part at depth. This is also visible from the deep moored current meters at the two moorings at ~44°W and at 0°, 36°W. Meridional velocity variability with periods between 30 and 40 days dominates in the moored velocity data at 0°, 35°W; 0°, 23°W; and 0°, 10°W. The modeled meridional velocity variability shows similar periodicity at these locations. At 0°, 23°W below 3000 m observed meridional velocity varies dominantly on periods between 10 and 20 days. A similar signal is also visible in the model. However, here it is restricted to areas closer to the topography. Low vertical resolution in the model could be a reason for these differences. At the surface east of 10°W the modeled meridional velocity varies predominantly on short periods (10–20 days). This signal is also visible in the moored velocity data. However, in the observations the signal is restricted to the uppermost ADCP bins.

Because the mooring at 0°, 23°W provides the most extensive moored dataset in the equatorial Atlantic, we use these data to further evaluate the model's ability to simulate intraseasonal meridional velocity variability at the equator. To analyze the representation of TIWs in the model, the meridional velocities between 0 and 50 m are filtered for variability on intraseasonal time scales with periods shorter than 80 days. Afterward, the kinetic energy is calculated and averaged over depth to derive the seasonal cycle of intraseasonal meridional kinetic energy (Fig. 3). In both model and observations, a maximum in August and a minimum in April is visible. In the

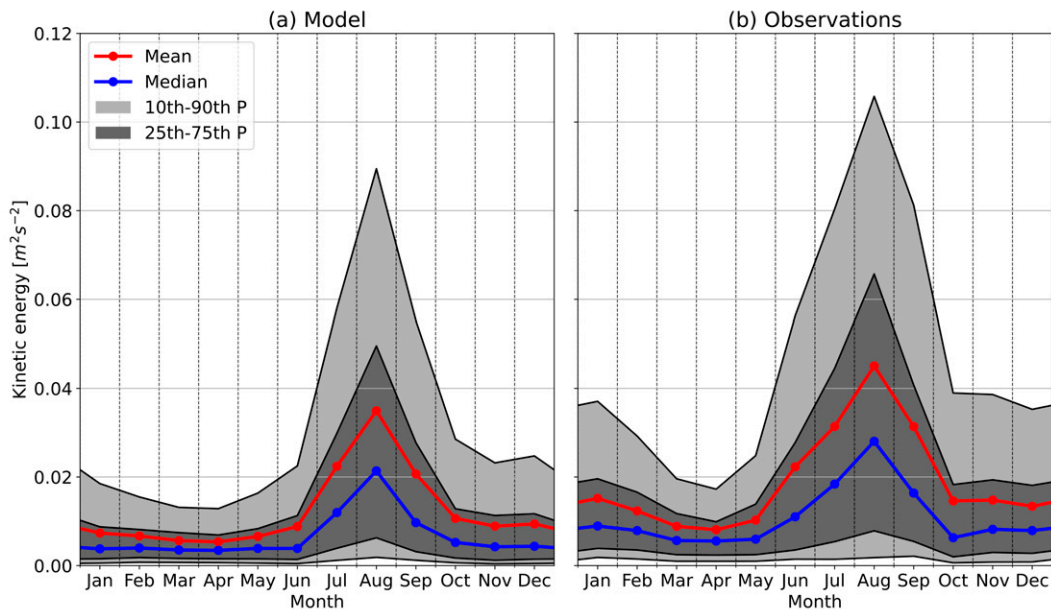


FIG. 3. The seasonal cycle of intraseasonal meridional kinetic energy ($\text{m}^2 \text{s}^{-2}$) at 0° , 23°W in (a) the model and (b) observations averaged between 0 and 50 m. The red line shows the monthly mean, and the blue line is the monthly median. The light- and dark-gray colored areas show the 10th–90th- and 25th–75th-percentile range derived from the distribution of monthly means.

observations, a secondary maximum is also found in January that is absent in the model. Additionally, the amplitude of the seasonal cycle is slightly weaker in the model than in the observations (about 12% in August). The distribution around the mean is comparable. In August, the 90th percentile in both model and observation is about 2 times the mean value.

The representation of intraseasonal variability at depth is investigated by calculating a spectrum of meridional velocity at 0° , 23°W . The periodogram of meridional velocity observed at 0° , 23°W reveals variance at the surface at all frequencies (Fig. 4a). There is also a distinct signal between the surface and 3000 m with frequencies between 6 and 15 cycles per year (periods of 25–60 days). Additionally, at depths between 3000 and 3500 m a low-frequency signal (1–3 cycles per year) as well as a high-frequency signal (25 cycles per year) is visible. The spectrum of the modeled meridional velocity is comparable in structure to the observations (Fig. 4b). The signal between the surface and 3000 m with frequencies between 6 and 15 cycles per year is present. The low-frequency signal between 3000 and 3500 m is also visible; however, the high-frequency signal around 25 cycles per year in this depth range is missing. The depth averages of the spectra between 100 and 3000 m show that the strength of the variance is comparable between model and observations on intraseasonal time scales (Fig. 4c). However, the model shows more variance on lower frequencies (~ 8 cycles per year) whereas the variance in the observations show more variability on higher frequencies (~ 12 cycles per year). Additionally, the model shows a very strong peak at 11 cycles per year that is not present in the observations. On longer time scales than intraseasonal periods, the observations exhibit stronger variance. Here, a distinct

peak at a period of 90 days is visible that is absent in the model. In contrast, the annual and semiannual peaks that are found in the model results are not present in the observations.

5. Characteristics of intraseasonal variability

a. Spectral structure

We calculate a frequency–wavenumber spectrum of the meridional velocity component of vertical modes to analyze the structure of intraseasonal variability along the equator. Here, we discuss the spectrum of mode-2 meridional velocity in detail as mode 2 exhibits the strongest Yanai-wave signal (see section 5b). The frequency–wavenumber spectrum shows elevated energy levels around the theoretical dispersion relation of Yanai waves (Fig. 5). The strongest signal is found between zonal wavenumbers of -0.25 and 0 cycles per degree (wavelengths larger than 450 km). Yanai waves with negative wavenumbers exhibit westward phase velocity, their group velocity and thus also their energy propagation is always eastward. Intraseasonal Yanai waves with small negative wavenumbers represent the dominant variability not only for mode 2, but in the frequency–wavenumber spectra of the barotropic mode and the first 15 vertical normal modes (not shown). There are also elevated levels of energy visible between the theoretical dispersion relations of Yanai waves and Rossby waves at around 10 cycles per year. These signals can be associated with TIWs (Farrar 2011).

b. Spatial distribution

In the upper ocean, the highest intraseasonal energy levels are visible near the western boundary (Fig. 2a). The maximum

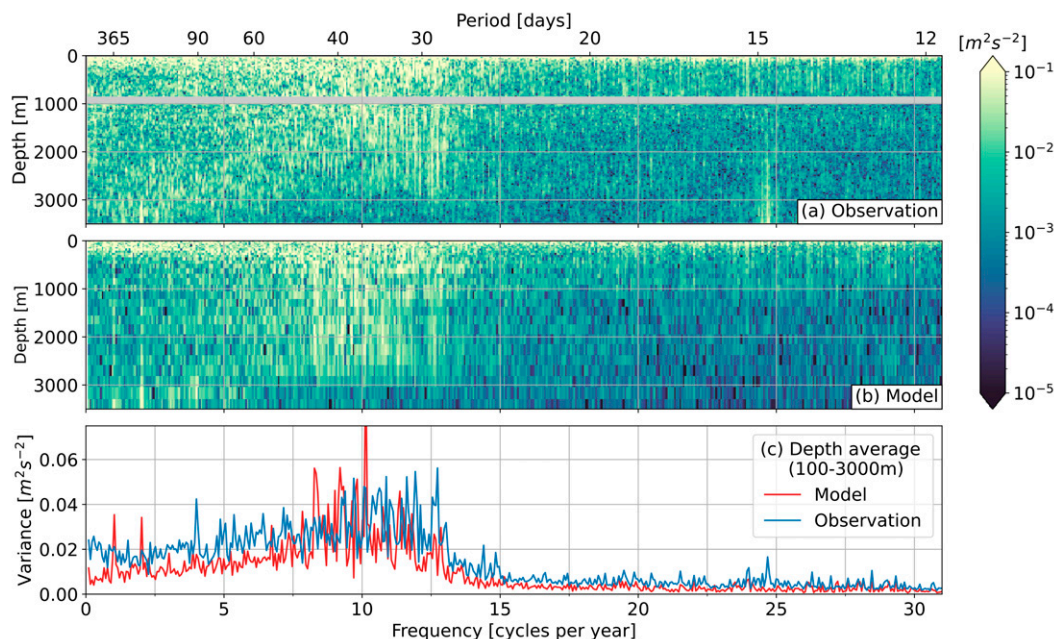


FIG. 4. Lomb-Scargle periodogram of meridional velocities at 0° , 23°W in (a) the model and (b) observations. Colors represent variance ($m^2 s^{-2}$). Depths that are too sparsely sampled are marked as gray. (c) Depth average between 100 and 3000 m of model (red) and observation (blue).

here is found at 42°W at a depth of 135 m. This region is located in the shear region between the North Brazil Current (NBC) and the EUC. From this region, a beam of enhanced energy is detectable reaching from the upper ocean to the ocean bottom

at about 20°W . Additionally, high energy levels are also found at the western boundary at depths between 1100 and 2500 m in the vicinity of the DWBC. In the eastern part of the basin, intra-seasonal energy levels are elevated at the surface and decrease

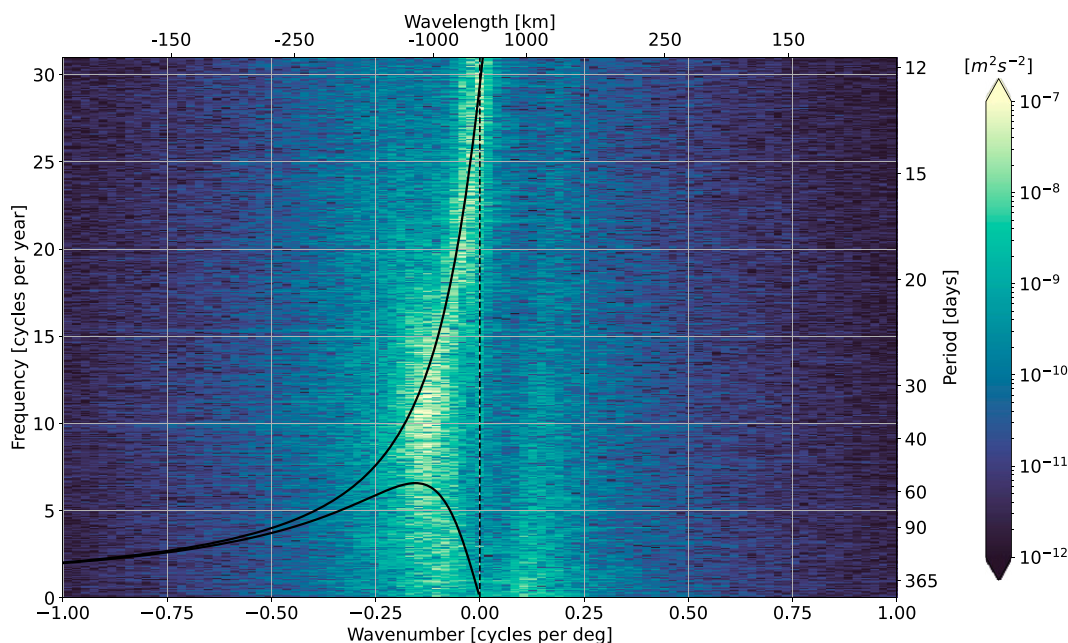


FIG. 5. The frequency-wavenumber spectra of modal amplitudes of meridional velocity of vertical mode 2 along the equator ($m^2 s^{-2}$). Note the logarithmic color scale. Black lines show the dispersion relation of Yanai waves and meridional mode-2 Rossby waves (from top to bottom). Note that only asymmetric ($l = 2, 4, 6, \dots$) Rossby waves have a meridional velocity component at the equator.

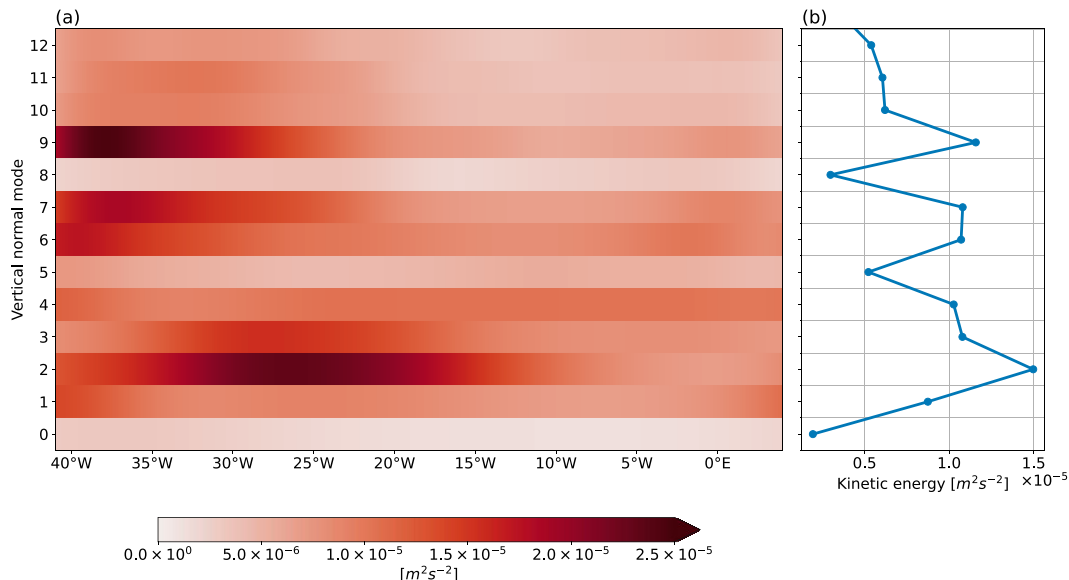


FIG. 6. The mean meridional kinetic energy of filtered modal velocity ($\text{m}^2 \text{s}^{-2}$) as a function of (a) longitude for vertical normal modes 0–12. Mode 0 represents the barotropic mode. (b) The mean meridional kinetic energy from the plot in (a) zonally averaged over all longitudes. Velocities are filtered for Yanai waves with zonal wavenumbers between -0.25 and -0.01 cycles per degree.

with depth. Additionally, high energy levels are found close to the topography at the eastern boundary. In contrast, low energy levels are found close to the topography between 15° and 25°W . Analyzing the topography in this region reveals shallow topographic features just north and south of the equator (Fig. 2a, gray line). These features are an obstacle for downward-propagating intraseasonal equatorial waves and can thus explain the low energy levels here.

To analyze the dominant intraseasonal period along the equator we consider, at each grid point along the equator, the period with maximum energy in the spectra on intraseasonal time scales (Fig. 2b). Periods from 30 to 50 days dominate over large areas along the equator. In the region of the energetic beam from the upper ocean near the western boundary to the bottom at around 20°W and east of it, periods between 30 and 40 days dominate. In the deep western part of the basin, variability with periods between 50 and 60 days is prevailing. At the surface east of 10°W , variability with periods between 10 and 20 days have the strongest signal. Close to the topography at the western boundary as well as at the Mid-Atlantic Ridge short periods (10–20 days) dominate. These signals likely can be explained by wave–topography interaction that leads to frequency shifts to higher frequencies.

The frequency–wavenumber analysis shows a clear signal of Yanai waves with negative wavenumbers along the equator (Fig. 5). To analyze the spatial distribution of the Yanai waves, we filter the modal velocities for the velocity field of these waves in space and time [see section 3c(2)]. Note again that the waves discussed in this study do not consist of a single baroclinic mode. Discussing the baroclinicity of these waves focuses on discussing what part of the vertical mode spectrum

is enhanced and thus gives information on the vertical structure of the waves.

The mean kinetic energy of the Yanai wave velocities reveals differences in strength and spatial distribution between the modes (Fig. 6). On average, mode-2 Yanai waves are the most energetic ones (Fig. 6b). They are predominantly active between the western boundary and about 10°W with the maximum kinetic energy found at 26°W . Mode-3 Yanai waves also have their maximum in kinetic energy located at about 26°W . However, they are much weaker than mode-2 Yanai waves. Mode-4, mode-6, mode-7, and mode-9 Yanai waves exhibit elevated activity close to the western boundary. Here, mode-7 and mode-9 Yanai waves are especially energetic, their energy levels rapidly drop east of 20°W . For higher modes the kinetic energy levels are comparably low. Overall, the spatial distribution of the kinetic energy of Yanai waves suggests different sources for the Yanai waves of different baroclinic structure.

Low-mode Yanai waves (mode 2–3) are most active in other regions than high-mode Yanai waves (mode 6–9). We further discuss these differences by considering Hovmöller plots of the velocity fields of the most energetic low-mode Yanai wave (mode 2) and the most energetic high-mode Yanai wave (mode 9) (Fig. 7). Mode-2 Yanai wave activity between 1995 and 2000 is found predominantly between the western boundary and 10°W . The wave packets propagate eastward over long distances before dissipating. Especially energetic Yanai waves are present in 1996. Here, Yanai wave energy propagates across the whole width of the Atlantic. The velocity field of mode-9 Yanai waves appears to be noisier than that of mode-2 Yanai waves. In general, packets of mode-9 Yanai waves have a smaller zonal coherence. They also do not propagate zonally

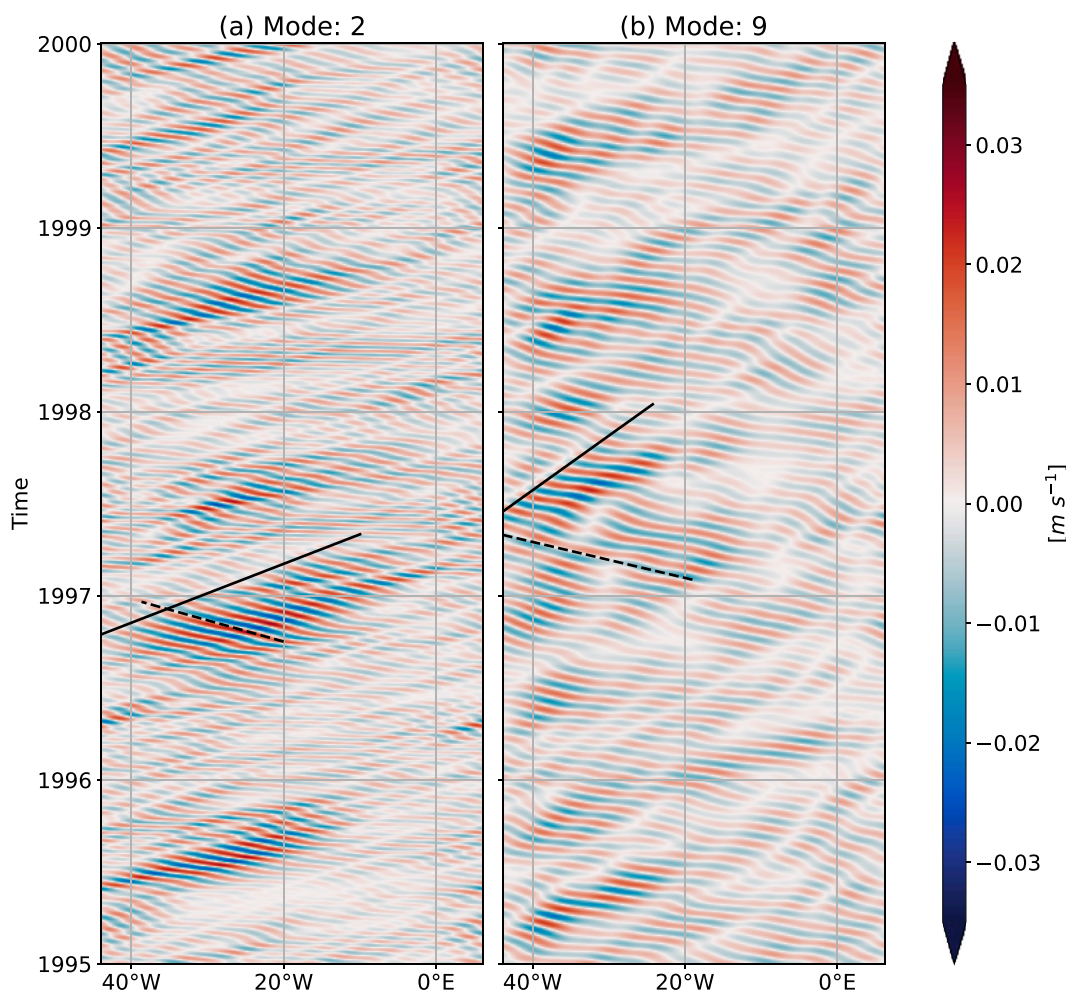


FIG. 7. Hovmöller plot of filtered meridional velocity of (a) mode 2 and (b) mode 9. Velocities are filtered for Yanai waves with zonal wavenumbers between -0.25 and -0.01 cycles per degree. The black dashed line illustrates westward phase velocities, and the black solid line shows eastward group velocities of a Yanai wave with a period of (a) 30 and (b) 36 days.

as far as mode-2 Yanai waves. Energetic mode-9 Yanai waves are found between the western boundary and 20°W .

c. Temporal variability

To analyze the temporal variability of Yanai waves we calculate the seasonal cycle of kinetic energy of the velocity field of Yanai waves with zonal wavenumbers between -0.25 and -0.01 cycles per degree. Averaging over all modes, a minimum in wave activity in February and a maximum in August are found. However, the seasonal cycles of the individual modes differ (Fig. 8). The seasonal cycles of low-mode Yanai waves (mode 1–3) show a clear maximum in August and a minimum in March/April. In contrast, the maximum of mode-7 Yanai waves is found in May. Note that the amplitude of the seasonal cycle of mode-7 Yanai waves is much smaller than the seasonal cycles of mode 1–3. The seasonal maximum of mode-9 Yanai wave activity is found in September and a secondary maximum is present in May. The analysis of the seasonal cycle

of Yanai wave activity further supports the hypothesis of different sources for Yanai waves of the different vertical structure. Especially, lower-mode Yanai waves (mode 1–3) show a different behavior than higher-mode Yanai waves (mode 7–9).

Despite the seasonal preference described above, the Hovmöller plots of the velocity fields of mode-2 and mode-9 Yanai waves reveal interannual variability of the wave activity (Fig. 7). The strong year-to-year variability also becomes evident when comparing the three snapshots of meridional velocity (Figs. 1b–d).

6. Sources and pathways of intraseasonal variability

The analyses of spatial and temporal characteristics of Yanai waves show distinct differences with respect to their baroclinic modes. This suggests that there are likely different sources of intraseasonal Yanai waves. Here, we analyze three possible source regions that we identify by considering high

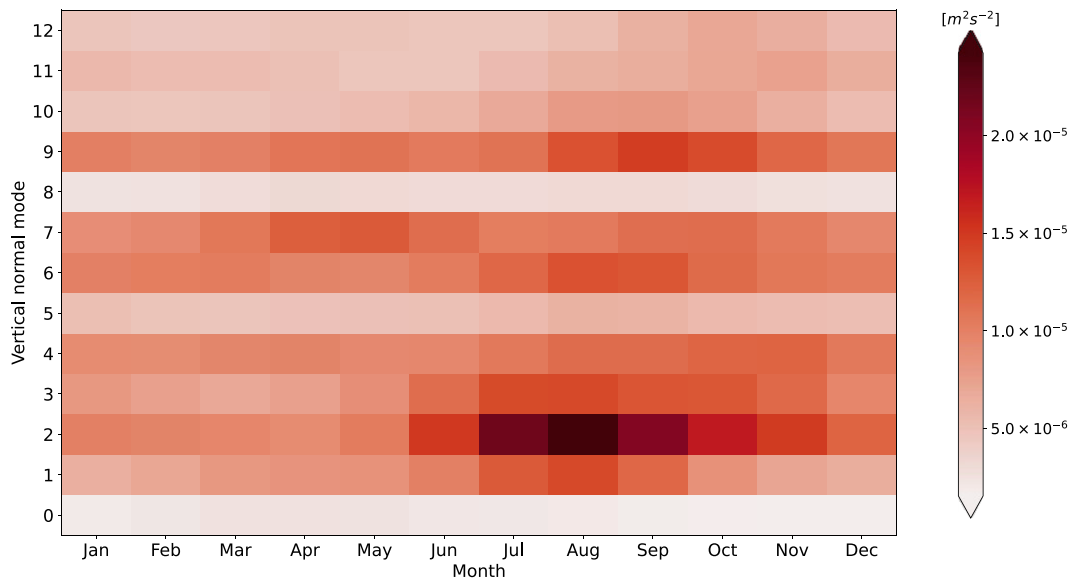


FIG. 8. The seasonal cycle of meridional kinetic energy of modal velocity that is filtered for Yanai waves with zonal wavenumbers between -0.25 and -0.01 cycles per degree. The modal velocity is zonally averaged along the equator.

energy levels in the equatorial section of mean meridional intraseasonal kinetic energy (Fig. 2a):

- 1) The first source region with high meridional intraseasonal kinetic energy levels is the Near Surface Intraseasonal Variability (NSIV) region that is defined as the upper 50 m along the equator across the basin.
- 2) The second region is located between the North Brazil Current and the Equatorial Undercurrent. The NBC/EUC shear region spans from 44° to 36°W between 60 and 260 m depth (Fig. 9).
- 3) The third region is also located at the western boundary but at middepth. This region is in the vicinity of the DWBC from 44° to 38°W and between 1100 and 2500 m depth (Fig. 9).

To analyze the vertical structure of the waves that are excited in the different source regions, we calculate the wavenumber–frequency spectra within the regions (Fig. 10). We compare these spectra with the theoretical dispersion relation of Yanai waves. Note that the wavenumber–frequency structure in the source region does not necessarily agree with the structure of free waves eventually found away from the source region. Additionally, the vertical structure of the forcing has to be considered as a vertically narrower forcing projects on a broader spectrum of vertical normal modes than a vertically wider forcing that favors low baroclinic modes.

The frequency–wavenumber spectrum of the NSIV exhibits the highest variance on intraseasonal time scales, with negative wavenumbers between -0.2 and 0 cycles per degree (Fig. 10a). Comparing the spectra with the theoretical dispersion relations of Yanai waves suggests that enhanced variance levels of NSIV projects rather on low-mode Yanai waves. This is further supported by the similarity of the seasonal cycle of intraseasonal kinetic energy of the NSIV (not shown) and the corresponding

seasonal cycle of Yanai waves of modes 1–3 (Fig. 8). Note that similar but weaker seasonal cycles are also visible in higher-mode Yanai waves (e.g., mode 6). This suggests that waves excited in the NSIV region consist of a superposition of different vertical modes. However, the main signal corresponds to a low-mode structure. Additionally, we analyze the NSIV as a function of longitude by calculating spectral analysis in time at each grid point along the equator (not shown). The NSIV consists mainly of two signals. Between the western boundary and 10°W a strong signal with a period of about 30 days is found. East of 10°W a weaker high-frequency signal is visible (~ 16 days). The longitudinal range of the 30-day signal fits very well to the longitudinal range of mode-2 Yanai wave activity (Fig. 6).

We further investigate which part of the subsurface intraseasonal variability can be explained by downward-propagating Yanai waves from the NSIV region by constructing theoretical Yanai beams. We construct theoretical Yanai beams with a period of 30 days starting at 20-m depth at the western boundary (44°W) and at 10°W (Fig. 9). It becomes evident that Yanai waves excited by NSIV can reach a vast subsurface region of the equatorial Atlantic. However, high intraseasonal energy levels at larger depths in the west cannot be explained by Yanai waves propagating downward from the surface. Additionally, we construct a Yanai beam with a period of 16 days starting at the surface at 10°W . Note that, in general, the higher the wave frequency, the steeper the slope of the Yanai beam [see Eq. (6)]. This beam shows that high-frequency Yanai waves excited east of 10°W are able to explain elevated energy levels near the eastern boundary.

In summary, the analysis above shows that NSIV is a viable source of intraseasonal Yanai waves. Analysis in the frequency–wavenumber space reveals that waves excited by the NSIV primarily are of low-baroclinic-mode structure. This hypothesis is

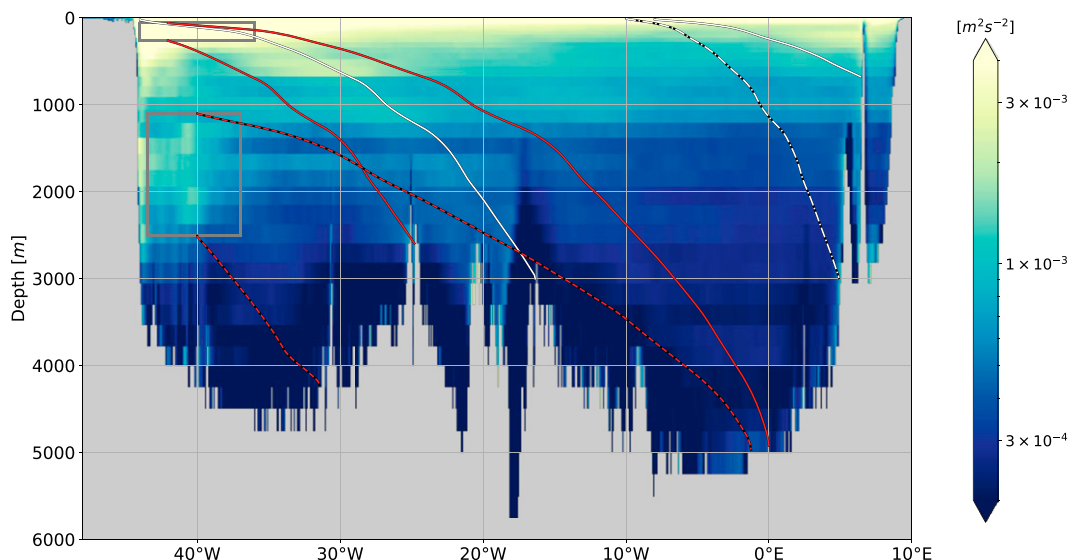


FIG. 9. Mean meridional intraseasonal kinetic energy along the equator; ($\text{m}^2 \text{s}^{-2}$) (color shading). The gray-outlined boxes display the extent of the NBC/EUC (upper box) and DWBC (lower box) source region. Lines represent theoretically constructed Yanai beams. White solid lines show waves with a period of 30 days excited at 20-m depth at 44° and 8°W . The gray dashed-dotted line represents a Yanai beam with a period of 16 days excited at the surface at 10°W . Red solid lines are Yanai waves with periods of 30 and 40 days excited at 42°W at 260 and 60 m, respectively. Red dashed-dotted lines show waves with periods of 80 and 40 days excited at 40°W at 1100- and 2500-m depth, respectively.

supported by the similarity of the seasonal cycle of the NSIV and low-mode Yanai waves. Yanai waves with a period of 30 days excited at the surface can be made responsible for a large fraction of the intraseasonal variability below the surface. However, a large part of the wave energy found in the west located at greater depths cannot be explained by it. Elevated intraseasonal energy levels near the eastern boundary can be explained by Yanai beams with shorter periods.

The NBC/EUC region is a region of strong meridional and zonal shear. The NBC is flowing northwestward along the boundary of Brazil. After crossing the equator, a part of the NBC retroflects into the EUC. Thus, the EUC is coming from the north and turns eastward at the equator at about 40°W (Schott et al. 2002).

Frequency–wavenumber analyses of the NBC/EUC shear region show variability with negative wavenumbers on intraseasonal to interannual time scales (Fig. 10b). The highest variance is found at periods between 30 and 60 days with wavenumbers of about -0.125 cycles per degree. Note that because of the smaller horizontal extent the wavenumber resolution is lower than in the frequency–wavenumber spectrum of NSIV. Because of the low frequency resolution of the spectrum, an attribution of the derived spectrum to theoretical dispersion relations is ambitious. Nevertheless, the longitudinal distribution of kinetic energy of Yanai waves suggests that the waves excited here are of high-mode structure (Fig. 6). Especially, mode-7 and mode-9 Yanai waves have high energy levels close to the western boundary.

The seasonal cycle of intraseasonal variability in the NBC/EUC region shows elevated activity between March and

August with a maximum in July (not shown). The amplitude of the seasonal cycle is much smaller than the seasonal cycle of NSIV. The seasonal cycle of mode-7 Yanai waves has similar characteristics (Fig. 8). It has a maximum in May and elevated activity is found between February and July. The amplitude of the seasonal cycle of mode-7 Yanai waves is also considerably smaller than that of mode 1–3 Yanai waves. The seasonal cycle of mode-9 Yanai has two local maxima, one in May and one in August, which suggest that mode-9 Yanai waves are probably excited both in the NBC/EUC and the NSIV region. In general, the analysis of the seasonal cycle of intraseasonal variability in the NBC/EUC region shows that waves excited here are of higher baroclinic mode structure.

We construct theoretical Yanai beams from the NBC/EUC region to discuss the intraseasonal variability that can be explained by downward propagation of Yanai waves. Mode-7 and mode-9 Yanai waves with zonal wavenumbers of about -0.125 cycles per degree have periods between 30 and 40 days (Fig. 10b). Thus, we analyze a Yanai beam with a period of 30 days that is excited at the lower boundary of the NBC/EUC shear region (260 m) and a Yanai beam with a period of 40 days that is excited at the upper boundary (60 m). The beams are excited at 42°W , which is the longitude with the maximum intraseasonal energy in the NBC/EUC region (Fig. 9). The Yanai beams form an “envelope” for the downward-propagating signal of the mean meridional intraseasonal kinetic energy. The analysis shows that Yanai waves with periods between 30 and 40 days propagating eastward and downward encounter topographic features at $\sim 20^\circ\text{W}$ (see also Fig. 2a for the features in the vicinity of the equator). Note that the energy levels of

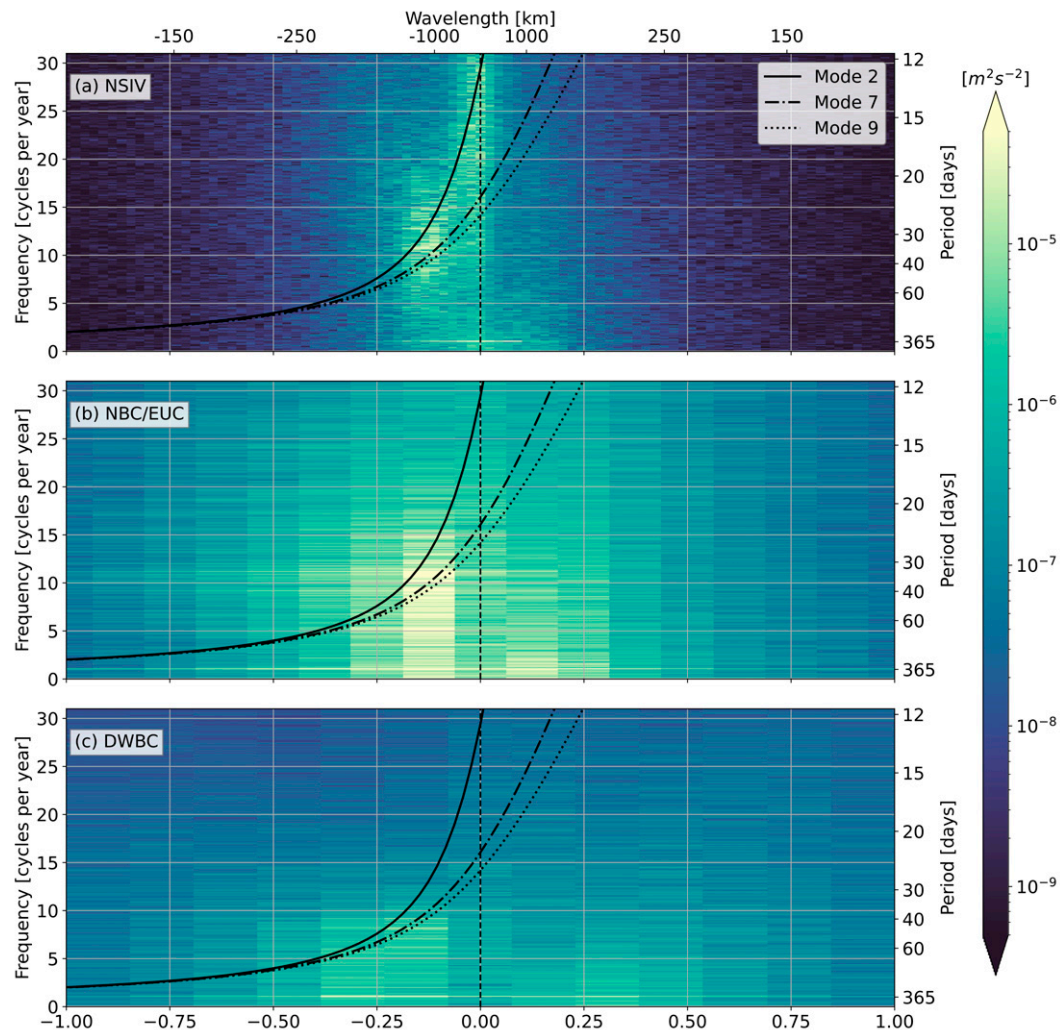


FIG. 10. The frequency–wavenumber spectra of meridional velocity in the proposed source regions (see the text and also Fig. 9 for a definition of these regions). Spectra are shown for (a) NSIV and for the intraseasonal variability of the (b) NBC/EUC and (c) DWBC. Spectra are calculated for each depth level of the source region at the equator in its longitude range and are averaged over depth afterward. For the definition of the depth and longitude range of each source region, refer to the text. Black lines represent the theoretical dispersion relations of Yanai waves of mode 2 (solid), mode 7 (dashed–dotted), and mode 9 (dotted).

mode-7 and mode-9 Yanai waves greatly decrease east of 20°W (Fig. 6). This supports the hypothesis that intraseasonal variability in the NBC/EUC region excites Yanai waves of high-baroclinic-mode structure.

In summary, a downward-propagating signal from the NBC/EUC source region at about 20°W is visible in the mean intraseasonal meridional kinetic energy and can be best explained by high-baroclinic-mode intraseasonal Yanai waves. Those waves have zonal wavenumbers of about -0.125 cycles per degree (wavelengths of ~ 900 km) and periods between 30 and 40 days. The dominant signals here are high-baroclinic-mode Yanai waves.

The region at the western boundary at middepth, close to the DWBC, shows enhanced levels of intraseasonal energy as well (Fig. 9). The energy levels are lower than those for the

NSIV or in the NBC/EUC regions. Looking at the mean velocity section shows that the highest intraseasonal variability is found just east of the DWBC, which flows southward along the continental slope.

The frequency–wavenumber spectrum calculated for this region reveals variability with negative wavenumbers on intraseasonal to longer periods (Fig. 10c). Elevated levels centered around -0.25 cycles per degree are evident. The variability in the DWBC region exhibits larger negative zonal wavenumbers than in the other source regions. In comparing with theoretical dispersion relations of Yanai waves, we suggest that it might project on Yanai waves with longer periods (between 40 and 80 days) and shorter wavelength (between 250 and 500 km). Little can be said about the vertical structure on which this signal projects, as the theoretical dispersion relations are similar

in this wavenumber range. However, the snapshot of modeled meridional velocity reveals velocity structures of large vertical extent that imply barotropic and low-baroclinic-mode activity (Fig. 1b). This is in agreement with the elevated barotropic and mode-1 Yanai wave energy near the western boundary (Fig. 6). Note that the dispersion relation of asymmetric ($l = 2, 4, 6, \dots$), low-baroclinic-mode Rossby waves would also fit to the elevated meridional kinetic energy levels in the frequency–wavenumber spectra in the DWBC. Short Rossby waves would also allow eastward energy propagation away from the western boundary. However, equatorial beams of such Rossby waves ($l = 2, 4, 6, \dots$) are much steeper than the ones of Yanai waves ($l = 0$) of the same periodicity [Eq. (6)]. Because intraseasonal energy levels are low in the corresponding regions, intraseasonal Rossby waves seem not to play an important role here.

Beams of Yanai waves with periods of 80 and 40 days respectively originating from the upper and lower boundary of the DWBC region demonstrate that Yanai waves excited here can explain elevated intraseasonal energy levels in the deep western part of the basin (Fig. 9). Waves excited in the upper part of the DWBC region are able to pass the Mid-Atlantic Ridge and reach the eastern basin at depth. Note that Yanai waves excited in the DWBC region can also propagate their energy upward. However, upward-propagating Yanai waves are masked by more-energetic Yanai waves from the upper ocean and are hardly detectable.

In summary, the DWBC region seems to be a source region for intraseasonal variability along the equator. However, the energy levels associated with the DWBC are lower than in the other source regions. Yanai wave energy that is shed from the DWBC region propagates eastward with flatter downward propagation as the periods of the waves excited here are longer [see Eq. (6)].

7. Summary and discussion

In this study, intraseasonal variability of the meridional velocity in the equatorial Atlantic Ocean is analyzed using the output of a high-resolution ocean general circulation model. The model is able to reproduce the structure and strength of observed meridional intraseasonal variability at the equator and is therefore a useful tool to investigate possible sources and pathways of the intraseasonal variability.

The main findings of the study are as follows:

- 1) The intraseasonal meridional velocity variability in the equatorial Atlantic can mostly be explained by Yanai waves of the first 12 vertical normal modes with zonal wavenumbers between -0.25 and -0.01 cycles per degree (wavelength larger than 450 km). Yanai waves of mode 2 exhibit the strongest signal.
- 2) The baroclinic structure of Yanai waves and their spatial distribution varies along the equator. Low-baroclinic-mode Yanai waves are mostly active between the western boundary and 10°W with a maximum at $\sim 26^\circ\text{W}$. High-baroclinic-mode Yanai waves show highest activity west of 20°W .

- 3) The Yanai wave activity along the equator exhibits a large interannual variability. However, a seasonal preference is still visible. Yanai waves of mode 1–3 have a distinct seasonal cycle with a maximum in August. The seasonal cycle of mode-7 Yanai waves has a smaller seasonal amplitude and a maximum in May.

- 4) Three regions are identified and analyzed as likely generation sites of intraseasonal Yanai waves:

- (i) NSIV is primarily associated with the excitation of low-baroclinic-mode Yanai waves (modes 1–3). Waves excited near the surface dominate the intraseasonal variability of vast subsurface regions along the equator.
- (ii) High-baroclinic-mode Yanai waves are excited in the shear region between the NBC/EUC. Corresponding wave energy propagates downward and eastward to reach the bottom at about 20°W . The downward propagation is dominated by high-baroclinic-mode Yanai waves.
- (iii) A region close to the DWBC exhibits elevated intraseasonal energy levels as well. Yanai waves excited here have shorter wavelengths and longer periods than in the other regions. The waves excited near the DWBC are less energetic than the waves from the other two source regions.

Our results show that the NSIV region is an important source region of intraseasonal variability at depth. The NSIV consists mainly of two signals: Between the western boundary and 10°W a strong signal centered around 30-day period is found. East of 10°W a weaker signal with periods of ~ 16 days is present. The periodicity and seasonality of the 30-day signal fits well to the characteristics of TIWs (Weisberg and Weingartner 1988; Athie and Marin 2008; Tuchen et al. 2018; Specht et al. 2021). This suggests that TIWs excite low-baroclinic-mode Yanai waves, their energy is propagating downward and eastward from the surface. Note that Tuchen et al. (2018) identified in the mooring data taken at 0° , 23°W Yanai waves dominantly of mode 2–5 with periods of 30–40 days. These findings agree well with the low-baroclinic-mode signal discussed in this study. The longitude range and periodicity of the high-frequency signal east of 10°W agree with observed Yanai waves forced directly by meridional wind fluctuations (Athie and Marin 2008; de Coëtlogon et al. 2010). Their wave energy propagates downward and eastward. Upon reaching the eastern boundary they may propagate poleward as coastally trapped waves (Guiavarc’h et al. 2008).

The model results suggest that high-baroclinic-mode Yanai waves with periods of 30–40 days are excited in a region between the NBC and the EUC. These waves are most likely generated by flow instabilities associated with the meridional and zonal shear between the two currents. However, further analyses of the exact mechanism have to be conducted. This is of interest as the waves are energetic and play a key role in transporting intraseasonal wave energy into the deep ocean. Note that the NBC/EUC shear region has so far been overlooked as a source region for deep intraseasonal variability although indicated in the maps of barotropic instability shown for the near

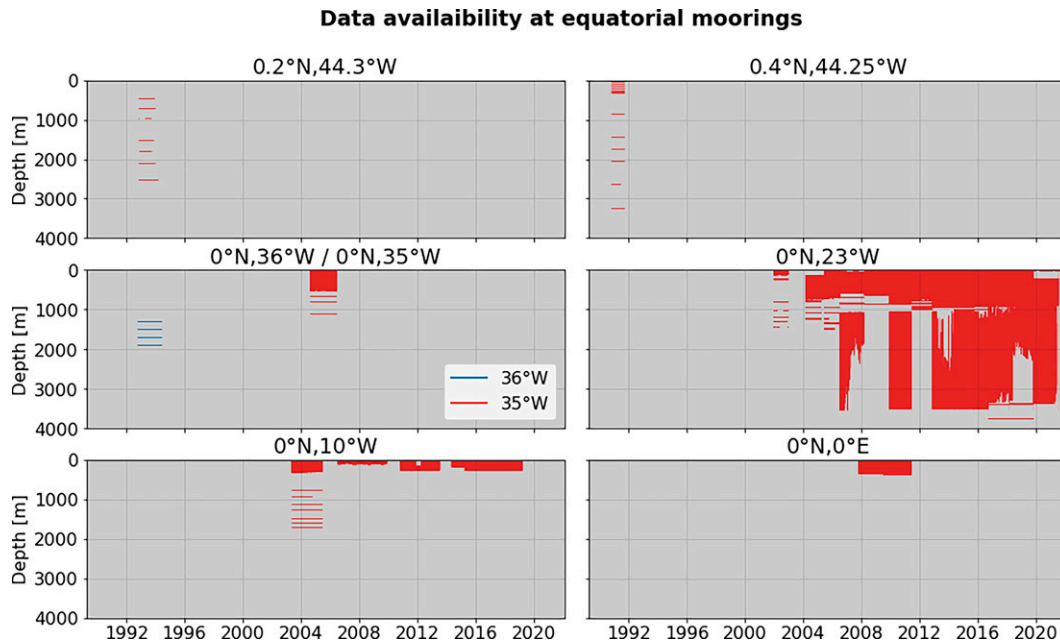


FIG. A1. The colored area gives an overview of available velocity data from equatorial moorings at different locations given in the title of the respective panels.

surface layer (upper 50 m) by von Schuckmann et al. (2008). Tuchen et al. (2018) found a signal of intraseasonal energy at depth that cannot be explained by downward-propagating Yanai beams originating near the surface. Waves excited in the lower part of the NBC/EUC region possibly represent the source for the deep energy found in the mooring data at 23°W.

Yanai waves excited near the DWBC have longer periods and shorter wavelengths and thus flatter downward beams than Yanai waves excited near the surface. The waves are most likely excited by instabilities of the DWBC although a closer analysis of generation mechanism has to be conducted as well. Analyses of snapshots of meridional velocity as well as analyses of kinetic energy of Yanai waves suggest that the Yanai waves excited in the DWBC region are of low-baroclinic or barotropic mode. This conclusion can also be drawn from the observed equatorial section of meridional velocity (Fig. 1a). Observed moored velocities support the discussed difference in periodicity between intraseasonal variability near the surface and at depth of the DWBC (Fig. 2b).

The importance of intraseasonal variability for the dynamics of the equatorial Atlantic has been underlined by several studies (Hua et al. 2008; Ascani et al. 2015; Greatbatch et al. 2018; Bastin et al. 2020). Especially, the role of DEIV for EDJs and the EICS (also called EEJs) was pointed out (Cravatte et al. 2012, 2017; Ménesguen et al. 2019; Delpech et al. 2021), which in turn influences the distribution of tracers (Brandt et al. 2012; Delpech et al. 2020) and possibly regional climate variability (Brandt et al. 2011). However, modeling the intermediate and deep circulation still remains a challenge. In this context the need for the knowledge of structure and strength of DEIV has been pointed out (Ménésguen et al. 2019). We show that intraseasonal waves of different strength, frequency, and vertical structure are active in different parts of the

equatorial Atlantic. The consequences of this for the forcing and maintenance of the DEC has to be examined more closely in the future as previous model studies focused typically on one single intraseasonal wave type. For example, d'Orgeville et al. (2007), Hua et al. (2008), and Ménesguen et al. (2009) used short Yanai waves destabilizing in the western equatorial basin to generate EDJ-like structures. These waves resemble the waves excited in the DWBC region discussed in the present study. In contrast, in the simulations of Ascani et al. (2015) and Bastin et al. (2020) DEIV is associated with downward-propagating Yanai waves excited from TIWs. The present study shows that such waves are important for elevated intraseasonal energy levels in the deep ocean. Furthermore, we also show that the energy of high-baroclinic-mode Yanai waves propagates downward and eastward from the NBC/EUC region. However, open questions remain, such as: What are the exciting mechanisms of the intraseasonal wave in the different source regions? What are deterministic mechanisms for the year-to-year variability of DEIV? Do we expect long-term changes in the appearance of DEIV due to changes of the upper ocean stratification or of the wind-driven and thermohaline circulation? And what could be the consequences for the DEC and the distribution of tracers? These questions have to be addressed in the future to deepen the understanding of the DEIV as an energy source for the DEC.

Acknowledgments. This study was funded by EU H2020 under Grant Agreement 817578 TRIATLAS project and by the Deutsche Forschungsgemeinschaft through several research cruises with R/V *Meteor*, R/V *Maria S. Merian*, and R/V *Somme*. Moored velocity data were acquired in cooperation with the PIRATA project. We are grateful to two anonymous reviewers for their helpful comments and suggestions, which led to significant improvements of the paper.

Intraseasonal meridional kinetic energy [m^2s^{-2}]

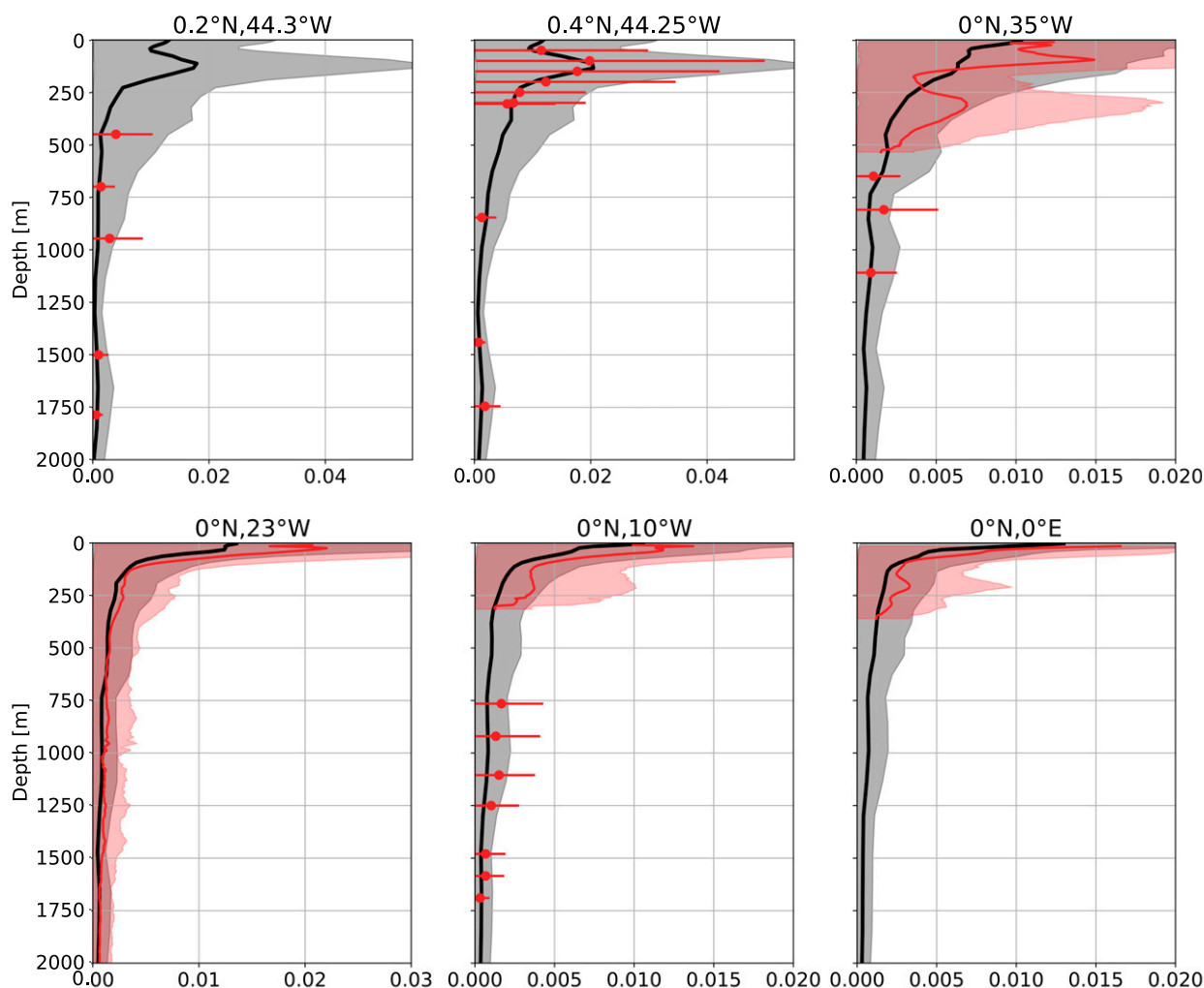


FIG. B1. Profiles of mean intraseasonal meridional kinetic energy at different mooring locations given in the title of the respective panels. Observations and model are presented in red and black, respectively. Shaded area/horizontal lines give the 10th–90th percentile of the distribution of intraseasonal meridional kinetic energy. Note the different extent of the horizontal axis.

Data availability statement. The observational data used in this study are publicly available. The velocity data collected at 0.2°N, 44.3°W and 0.4°N, 44.25°W can be accessed online (<https://www.ncei.noaa.gov/access/metadata/landing-page/bin/iso?id=gov.noaa.nodc:NODC-WOCE-GDR>; WOCE Data Products Committee 2002). Moored velocity data from the other location are also available online (<https://doi.org/10.1594/PANGAEA.946238>).

APPENDIX A

Moored Velocity Data from the Equator

Figure A1 provides a summary of available velocity data from equatorial moorings at the indicated locations.

APPENDIX B

Comparison of Modeled and Observed Intraseasonal Meridional Kinetic Energy

Profiles of mean intraseasonal meridional kinetic energy at the indicated mooring locations are provided in Fig. B1.

REFERENCES

- Ascani, F., E. Firing, P. Dutrieux, J. P. McCreary, and A. Ishida, 2010: Deep equatorial ocean circulation induced by a forced–dissipated Yanai beam. *J. Phys. Oceanogr.*, **40**, 1118–1142, <https://doi.org/10.1175/2010JPO4356.1>.
- , —, J. P. McCreary, P. Brandt, and R. J. Greatbatch, 2015: The deep equatorial ocean circulation in wind-forced numerical

- solutions. *J. Phys. Oceanogr.*, **45**, 1709–1734, <https://doi.org/10.1175/JPO-D-14-0171.1>.
- Athie, G., and F. Marin, 2008: Cross-equatorial structure and temporal modulation of intraseasonal variability at the surface of the tropical Atlantic Ocean. *J. Geophys. Res.*, **113**, C08020, <https://doi.org/10.1029/2007JC004332>.
- Bastin, S., M. Claus, P. Brandt, and R. J. Greatbatch, 2020: Equatorial deep jets and their influence on the mean equatorial circulation in an idealized ocean model forced by intraseasonal momentum flux convergence. *Geophys. Res. Lett.*, **47**, e2020GL087808, <https://doi.org/10.1029/2020GL087808>.
- Biaostoch, A., and Coauthors, 2021: Regional imprints of changes in the Atlantic meridional overturning circulation in the eddy-rich ocean model VIKING20X. *Ocean Sci.*, **17**, 1177–1211, <https://doi.org/10.5194/os-17-1177-2021>.
- Brandt, P., A. Funk, V. Hormann, M. Dengler, R. J. Greatbatch, and J. M. Toole, 2011: Interannual atmospheric variability forced by the deep equatorial Atlantic Ocean. *Nature*, **473**, 497–500, <https://doi.org/10.1038/nature10013>.
- , and Coauthors, 2012: Ventilation of the equatorial Atlantic by the equatorial deep jets. *J. Geophys. Res.*, **117**, C12015, <https://doi.org/10.1029/2012JC008118>.
- , M. Claus, R. J. Greatbatch, R. Kopte, J. M. Toole, W. E. Johns, and C. W. Böning, 2016: Annual and semiannual cycle of equatorial Atlantic circulation associated with basin-mode resonance. *J. Phys. Oceanogr.*, **46**, 3011–3029, <https://doi.org/10.1175/JPO-D-15-0248.1>.
- , and Coauthors, 2019: Trans-Atlantic Equatorial cruise I, Cruise No. M158, September 19–26 October 2019, Walvis Bay (Namibia)-Recife (Brazil). METEOR-Berichte M158, 48 pp., https://doi.org/10.2312/cr_m158.
- , and Coauthors, 2021: Atlantic Equatorial Undercurrent intensification counteracts warming-induced deoxygenation. *Nat. Geosci.*, **14**, 278–282, <https://doi.org/10.1038/s41561-021-00716-1>.
- Bunge, L., C. Provost, B. L. Hua, and A. Kartavtseff, 2008: Variability at intermediate depths at the equator in the Atlantic Ocean in 2000–06: Annual cycle, equatorial deep jets, and intraseasonal meridional velocity fluctuations. *J. Phys. Oceanogr.*, **38**, 1794–1806, <https://doi.org/10.1175/2008JPO3781.1>.
- Claus, M., R. J. Greatbatch, P. Brandt, and J. M. Toole, 2016: Forcing of the Atlantic Equatorial deep jets derived from observations. *J. Phys. Oceanogr.*, **46**, 3549–3562, <https://doi.org/10.1175/JPO-D-16-0140.1>.
- Cravatte, S., W. S. Kessler, and F. Marin, 2012: Intermediate zonal jets in the tropical Pacific Ocean observed by Argo floats. *J. Phys. Oceanogr.*, **42**, 1475–1485, <https://doi.org/10.1175/JPO-D-11-0206.1>.
- , E. Kestenare, F. Marin, P. Dutrieux, and E. Firing, 2017: Subthermocline and intermediate zonal currents in the tropical Pacific Ocean: Paths and vertical structure. *J. Phys. Oceanogr.*, **47**, 2305–2324, <https://doi.org/10.1175/JPO-D-17-0043.1>.
- de Coëtlogon, G., S. Janicot, and A. Lazar, 2010: Intraseasonal variability of the ocean – Atmosphere coupling in the Gulf of Guinea during boreal spring and summer. *Quart. J. Roy. Meteor. Soc.*, **136**, 426–441, <https://doi.org/10.1002/qj.554>.
- Delpéch, A., S. Cravatte, F. Marin, Y. Morel, E. Gronchi, and E. Kestenare, 2020: Observed tracer fields structuration by middepth zonal jets in the tropical Pacific. *J. Phys. Oceanogr.*, **50**, 281–304, <https://doi.org/10.1175/JPO-D-19-0132.1>.
- , C. Ménesguen, Y. Morel, L. N. Thomas, F. Marin, S. Cravatte, and S. Le Gentil, 2021: Intra-annual Rossby waves destabilization as a potential driver of low-latitude zonal jets: Barotropic dynamics. *J. Phys. Oceanogr.*, **51**, 365–384, <https://doi.org/10.1175/JPO-D-20-0180.1>.
- d’Orgeville, M., B. L. Hua, and H. Sasaki, 2007: Equatorial deep jets triggered by a large vertical scale variability within the western boundary layer. *J. Mar. Res.*, **65**, 1–25, <https://doi.org/10.1357/002224007780388720>.
- Farrar, J. T., 2011: Barotropic Rossby waves radiating from tropical instability waves in the Pacific Ocean. *J. Phys. Oceanogr.*, **41**, 1160–1181, <https://doi.org/10.1175/2011JPO4547.1>.
- , and R. A. Weller, 2006: Intraseasonal variability near 10°N in the Eastern Tropical Pacific Ocean. *J. Geophys. Res.*, **111**, C05015, <https://doi.org/10.1029/2005JC002989>.
- , T. Durland, S. R. Jayne, and J. F. Price, 2021: Long-distance radiation of Rossby waves from the equatorial current system. *J. Phys. Oceanogr.*, **51**, 1947–1966, <https://doi.org/10.1175/JPO-D-20-0048.1>.
- Fischer, J., and F. A. Schott, 1997: Seasonal transport variability of the deep western boundary current in the equatorial Atlantic. *J. Geophys. Res.*, **102**, 27 751–27 769, <https://doi.org/10.1029/97JC02327>.
- Gill, A. E., 1982: *Atmosphere–Ocean Dynamics*. International Geophysics Series, Vol. 30, Academic Press, 662 pp.
- Greatbatch, R. J., and Coauthors, 2018: Evidence for the maintenance of slowly varying equatorial currents by intraseasonal variability. *Geophys. Res. Lett.*, **45**, 1923–1929, <https://doi.org/10.1002/2017GL076662>.
- Grodsky, S. A., J. A. Carton, C. Provost, J. Servain, J. A. Lorenzetti, and M. J. McPhaden, 2005: Tropical instability waves at 0°N, 23°W in the Atlantic: A case study using Pilot Research Moored Array in the Tropical Atlantic (PIRATA) mooring data. *J. Geophys. Res.*, **110**, C08010, <https://doi.org/10.1029/2005JC002941>.
- Guiavarch, C., A. M. Treguier, and A. Vangriesheim, 2008: Remotely forced biweekly deep oscillations on the continental slope of the Gulf of Guinea. *J. Geophys. Res. Oceans*, **113**, C06002, <https://doi.org/10.1029/2007JC004471>.
- Hormann, V., and P. Brandt, 2009: Upper equatorial Atlantic variability during 2002 and 2005 associated with equatorial Kelvin waves. *J. Geophys. Res.*, **114**, C03007, <https://doi.org/10.1029/2008JC005101>.
- Hua, B. L., M. d’Orgeville, M. D. Fruman, C. Menesguen, R. Schopp, P. Klein, and H. Sasaki, 2008: Destabilization of mixed Rossby gravity waves and the formation of equatorial zonal jets. *J. Fluid Mech.*, **610**, 311–341, <https://doi.org/10.1017/S0022112008002656>.
- Jochum, M., P. Malanotte-Rizzoli, and A. Busalacchi, 2004: Tropical instability waves in the Atlantic Ocean. *Ocean Modell.*, **7**, 145–163, [https://doi.org/10.1016/S1463-5003\(03\)00042-8](https://doi.org/10.1016/S1463-5003(03)00042-8).
- Johns, W. E., P. Brandt, B. Bourlès, A. Tantet, A. Papapostolou, and A. Houk, 2014: Zonal structure and seasonal variability of the Atlantic Equatorial Undercurrent. *Climate Dyn.*, **43**, 3047–3069, <https://doi.org/10.1007/s00382-014-2136-2>.
- Johnson, G. C., and D. Zhang, 2003: Structure of the Atlantic Ocean equatorial deep jets. *J. Phys. Oceanogr.*, **33**, 600–609, [https://doi.org/10.1175/1520-0485\(2003\)033<0600:SOTAOE>2.0.CO;2](https://doi.org/10.1175/1520-0485(2003)033<0600:SOTAOE>2.0.CO;2).
- Madec, G., and NEMO Team, 2016: NEMO ocean engine. Note du Pôle de modélisation de l’Institut Pierre-Simon Laplace 27, 386 pp., https://www.nemo-ocean.eu/wp-content/uploads/NEMO_book.pdf.
- McCreary, J. P., 1984: Equatorial beams. *J. Mar. Res.*, **42**, 395–430, <https://doi.org/10.1357/002224084788502792>.

- Ménesguen, C., B. L. Hua, M. D. Fruman, and R. Schopp, 2009: Dynamics of the combined extra-equatorial and equatorial deep jets in the Atlantic. *J. Mar. Res.*, **67**, 323–346, <https://doi.org/10.1357/002224009789954766>.
- , A. Delpech, F. Marin, S. Cravatte, F. Schopp, and Y. Morel, 2019: Observations and mechanisms for the formation of deep equatorial and tropical circulation. *Earth Space Sci.*, **6**, 370–386, <https://doi.org/10.1029/2018EA000438>.
- Olivier, L., G. Reverdin, A. Hasson, and J. Boutin, 2020: Tropical instability waves in the Atlantic Ocean: Investigating the relative role of sea surface salinity and temperature from 2010 to 2018. *J. Geophys. Res. Oceans*, **125**, e2020JC016641, <https://doi.org/10.1029/2020JC016641>.
- Perez, R. C., R. Lumpkin, W. E. Johns, G. R. Foltz, and V. Hormann, 2012: Interannual variations of Atlantic tropical instability waves. *J. Geophys. Res.*, **117**, C03011, <https://doi.org/10.1029/2011JC007584>.
- Philander, S. G. H., 1978: Forced oceanic waves. *Rev. Geophys.*, **16**, 15–46, <https://doi.org/10.1029/RG016i001p00015>.
- Schott, F. A., P. Brandt, M. Hamann, J. Fischer, and L. Stramma, 2002: On the boundary flow off Brazil at 5–10°S and its connection to the interior tropical Atlantic. *Geophys. Res. Lett.*, **29**, 21-1–21-4, <https://doi.org/10.1029/2002GL014786>.
- Send, U., C. Eden, and F. Schott, 2002: Atlantic equatorial deep jets: Space–time structure and cross-equatorial fluxes. *J. Phys. Oceanogr.*, **32**, 891–902, [https://doi.org/10.1175/1520-0485\(2002\)032<0891:AEDJST>2.0.CO;2](https://doi.org/10.1175/1520-0485(2002)032<0891:AEDJST>2.0.CO;2).
- Specht, M. S., J. Jungclauss, and J. Bader, J., 2021: Identifying and characterizing subsurface tropical instability waves in the Atlantic Ocean in simulations and observations. *J. Geophys. Res. Oceans*, **126**, e2020JC017013, <https://doi.org/10.1029/2020JC017013>.
- Thomson, R. E., and W. J. Emery, 2014: Digital filters. *Data Analysis Methods in Physical Oceanography*, 3rd ed. R. E. Thomson, and W. J. Emery, Eds., Elsevier, 593–637, <https://doi.org/10.1016/B978-0-12-387782-6.00006-5>.
- Tsujino, H., and Coauthors, 2018: JRA-55 based surface dataset for driving ocean–sea-ice models (JRA55-do). *Ocean Modell.*, **130**, 79–139, <https://doi.org/10.1016/j.ocemod.2018.07.002>.
- Tuchen, F. P., P. Brandt, M. Claus, and R. Hummels, 2018: Deep intraseasonal variability in the central equatorial Atlantic. *J. Phys. Oceanogr.*, **48**, 2851–2865, <https://doi.org/10.1175/JPO-D-18-0059.1>.
- , and Coauthors, 2022: Two decades of full-depth current velocity observations from a moored observatory in the central equatorial Atlantic at 0°N, 23°W. *Front. Mar. Sci.*, **9**, 910979, <https://doi.org/10.3389/fmars.2022.910979>.
- von Schuckmann, K., P. Brandt, and C. Eden, 2008: Generation of tropical instability waves in the Atlantic Ocean. *J. Geophys. Res.*, **113**, C08034, <https://doi.org/10.1029/2007JC004712>.
- Weisberg, R. H., and T. J. Weingartner, 1988: Instability waves in the Equatorial Atlantic Ocean. *J. Phys. Oceanogr.*, **18**, 1641–1657, [https://doi.org/10.1175/1520-0485\(1988\)018<1641:IWITEA>2.0.CO;2](https://doi.org/10.1175/1520-0485(1988)018<1641:IWITEA>2.0.CO;2).
- Welch, P. D., 1967: The use of fast Fourier transform for the estimation of power spectra: A method based on time averaging over short, modified periodograms. *IEEE Trans. Audio Electroacoust.*, **15**, 70–73, <https://doi.org/10.1109/TAU.1967.1161901>.
- WOCE Data Products Committee, 2002: NODC standard product: World Ocean Circulation Experiment (WOCE) Global Data Resource (GDR), versions 1-3. Subset: Current Meter, NOAA National Centers for Environmental Information, accessed 10 April 2022, <https://www.ncei.noaa.gov/archive/accession/NODC-WOCE-GDR>.
- Youngs, M. K., and G. C. Johnson, 2015: Basin-wavelength equatorial deep jet signals across three oceans. *J. Phys. Oceanogr.*, **45**, 2134–2148, <https://doi.org/10.1175/JPO-D-14-0181.1>.
- Zhang, Z., L. J. Pratt, F. Wang, J. Wang, and T. Shuwen, 2020: Intermediate intraseasonal variability in the western tropical Pacific Ocean: Meridional distribution of equatorial Rossby waves influenced by a tilted boundary. *J. Phys. Oceanogr.*, **50**, 921–933, <https://doi.org/10.1175/JPO-D-19-0184.1>.